UNIVERSIDADE DE LISBOA
FACULDADE DE CIÊNCIAS

DEPARTAMENTO DE ENGENHARIA GEOGRÁFICA, GEOFÍSICA E ENERGIA

Effects of initial plate conditions on subduction process: numerical and laboratory experiments

Sílvia Salvador Duarte

Dissertação
Mestrado em Ciências Geofísicas
Especialização em Geofísica Interna

2014

UNIVERSIDADE DE LISBOA
FACULDADE DE CIÊNCIAS

DEPARTAMENTO DE ENGENHARIA GEOGRÁFICA, GEOFÍSICA E ENERGIA

Effects of initial plate conditions on subduction process: numerical and laboratory experiments

Sílvia Salvador Duarte

Dissertação
Mestrado em Ciências Geofísicas
Especialização em Geofísica Interna

Orientadores: Doutora Catherine Mériaux e Doutor Dave A. May

2014

Acknowledgements

I would like to thank Dr. Catherine Mériaux and Dr. Dave May for having accepted to be my advisers during this final stage of my Master degree. A very special thank you to all of my friends and colleagues who accompanied me in this journey, and to my family who have always supported me and provided me the opportunity to pursue an academic degree, to especially my brother that, against all odds, gave me the most support by always cheering me up.

Abstract (resumo em inglês)

Subduction process is investigated with laboratory and numerical experiments in a three-dimensional approach. The experiments model the sinking of a dense plate initially resting on top of a less dense deep mantle, with a tip bent downwards, and the process is entirely driven by the negative buoyancy due to density contrast. Subduction initiation is not modelled and a no overriding plate system is assumed. Both laboratory and numerical models assume a free surface at the top. Laboratory experiments are set with a trailing plate fixed at one edge and numerical experiments are set with a free trailing edge and benchmarked with the laboratory work of Schellart [2008], in particular with the experiment 8. The sinking velocity of the slab tip is investigated, the main goal is to test its dependency on the initial conditions: initial slab tip length (l_0) and initial dipping angle (θ_0). A steady state stage is identified before the slab tip reaches the bottom and sinking velocities are estimated for this particular stage for all experiments. Laboratory results show that the initial conditions do not impact significantly the sinking velocity for a free trailing plate. By contrast, the numerical results show that there is a relation between the initial slab tip length and the sinking velocity, moreover, that the impact of the initial slab tip dipping angle is much less important. All experiments show trench retreat and the numerical simulations exhibit a toroidal mantle flow pattern around the slab lateral borders and a two-cell poloidal pattern without mass transport around the slab tip. There is also a significant difference on the plate kinematics and dynamics as it sinks between the fixed and free trailing edge approaches. Finally, the comparison of the numerical results with the Schellart [2008] experiment demonstrates that a benchmark between three-dimensional, free surface laboratory and numerical models, with a free trailing edge, is not accomplished.

Key-words: tectonophysics, subduction, sinking velocities, plate dynamics

Resumo (resumo em Português)

Com este trabalho pretende-se estudar o processo de subducção de uma placa tectónica com recurso a modelos laboratoriais e numéricos, utilizando uma abordagem tridimensional. Os modelos foram escalados de modo a poderem ser considerados dinamicamente semelhantes um modelo de um limite de convergência de placas tectónicas na Natureza. As diferentes experiências executadas são simulações do afundamento de uma placa litosférica densa e com viscosidade elevada, que inicialmente se encontra em repouso sobre o manto, de densidade e viscosidade inferiores, com uma das suas extremidades dobrada para o interior do manto. O sistema parte do repouso, i.e., não existe forçamento devido forças inerciais, pelo que o processo é completamente impulsionado pelo contraste de densidades entre a placa e o manto. É utilizado, nos dois tipos de modelo, um manto análogo completo sem descontinuidades, i.e., considera-se um manto completamente uniforme em todo o seu interior e limitado no fundo pela fronteira com o núcleo terrestre. O processo que inicia a subducção não é modelado, pois o objectivo deste trabalho prende-se com a evolução do processo e não com o modo como este é iniciado. Também não são tidas em conta quaisquer variações de fase e temperatura do material, assume-se que o fluído que representa o manto é incompressível e que é caracterizado por um número de Prandtl infinito, pelo que o momento é difundido mais rapidamente que o calor. Para simplificação do sistema assume-se, ainda, que não existe uma segunda placa para debaixo da qual a primeira é subduzida, este pressuposto implica que a resistência nos limites da placa é baixa. Neste estudo simula-se uma superfície livre no topo do manto, tanto nos modelos laboratoriais como nos numéricos, ou seja, a formação de topografia não é constrangida (nos modelos numéricos encontrados na literatura é frequentemente utilizada uma camada fina lubrificante por cima da placa, pelo que a fronteira

entre o topo e a atmosfera é rígida). As experiências laboratoriais são caracterizadas por um contraste de densidades de $\Delta\rho = \rho_p - \rho_m = 99$ kg·m^{-3}, entre placa e manto, e uma razão entre viscosidades de $\gamma = \eta_p/\eta_m = 640$ (os ìndices 'p' e 'm' denotam placa e manto), nestas experiências a placa encontra-se fixada na extremidade oposta àquela que afunda. Este cenário é comparável a sistemas de subducção naturais nos quais se verifica que a fossa, zona onde a placa que está a ser subduzida começa a penetrar o manto, tem uma velocidade de recuo significativamente mais elevada que a velocidade da parte placa que é arrastada à superfície e que se move em direcção à fossa. As simulações numéricas são caracterizadas por um contraste de densidades e uma razão entre viscosidades ligeiramente inferiores, 80 kg·m^{-3} e 253.3, respectivamente. Nestas experiências a placa é definida com a extremidade livre, permitindo a movimentação da parte da placa que se encontra à superfície no sentido da fossa. Este cenário é representativo de sistemas naturais nos quais existe uma zona de divergência na extremidade da placa, como, por exemplo, uma crista média oceânica. As simulações numéricas têm como referência as experiências laboratoriais de Schellart [2008], especialmente a experiência 8, que se trata também de um modelo de manto completo. O código responsável pelas simulações numéricas foi construído de modo a se aproximar o melhor possível desta experiência com o objectivo de se obter resultados semelhantes entre trabalho laboratorial e numérico numa abordagem 3-D e utilizando modelos com uma superfície livre no topo, o que é inovador, pois até agora a correspondência entre resultados laboratoriais e numéricos utilizando modelos de superfície livre foi apenas feita com sucesso por Schmeling et al. [2008] numa abordagem bidimensional, na qual muitos efeitos do processo de subducção são suprimidos. O estudo centra-se na velocidade de afundamento da ponta da placa, sendo o principal objectivo deste trabalho verificar se existe uma relação entre esta e as condições iniciais definidas para o comprimento (l_0) e ângulo (θ_0) iniciais de mergulho da extremidade da placa, portanto, diferentes valores para as duas variáveis são testados, mantendo os restantes parâmetros que caracterizam os modelos constantes. É identificada uma fase no processo de subducção na qual a ponta da placa afunda de modo estacionário até alcançar o fundo do manto, e analisada detalhadamente, sendo que é para esta fase que a velocidade de afundamento é estimada, pois é quando pode ser considerada praticamente constante. Os resultados laboratoriais mostram que as condições iniciais não têm um impacto significativo na velocidade de afundamento. É possível ainda verificar que o bordo lateral da ponta da placa afunda a uma velocidade inferior à velocidade estimada para o centro da ponta da placa, o que é justificado pelo facto de os bordos laterais serem mais afectados por efeitos de arraste por parte do manto e se mantifesta pela forma curva que a fossa assume durante o processo. Por outro lado, os resultados numéricos mostram que a velocidade de afundamento aumenta para valores do comprimento inicial da extremidade mais elevados, mas diminui para valores do ângulo de mergulho inicial superiores. Além disso, estes resultados mostram que o impacto na velocidade de afundamento da placa devido a variações no ângulo inicial são muito menores que o impacto devido a variações no comprimento inicial da extremidade mergulhante. Estes contrastes entre resultados permitem concluir que mantendo a placa fixa numa das extremidades não há influência das condições iniciais mas no caso de a placa ter a extremidade livre as condições inicias influenciam bastante o modo como a subducção evolui, nomeadamente, a velocidade com que a ponta da placa afunda durante a fase estacionária do processo. Em todas as experiências verifica-se que a fossa não é estática durante o processo, tem um movimento de recuo. Este movimento também apresenta uma fase estacionária, que ocorre simultaneamente à identificada para o afundamento da ponta da placa, sendo por isso igualmente possível estimar velocidades de recuo para cada experiência. Verifica-se que o recuo é mais intenso nas experiências laboratoriais, ou seja no caso de uma placa fixa na extremidade.

As experiências numéricas revelam que o recuo da fossa também é influenciado pelas condições iniciais, o aumento do comprimento inicial da ponta da placa implica menores velocidade de recuo, assim como a diminuição do ângulo de mergulho inicial. Relativamente à evolução das posições do material do manto enquanto a placa afunda, nas experiências numéricas, é possível verificar que se forma uma corrente de retorno no manto com um padrão toroidal em torno dos bordos laterais da ponta placa, com transporte de massa entre a zona por baixo da placa para a cunha de manto em torno dos bordos da placa. Verifica-se ainda um sistema poloidal de retorno constituído por duas células em torno da ponta da placa, no qual uma célula localiza-se por baixo da placa e a outra na cunha de manto, mas sem transporte de massa entre as células. Finalmente, a comparação entre os resultados numéricos e a experiência de Schellart [2008] demonstra que o uso de modelos laboratoriais como referência para construção de modelos numéricos, utilizando a abordagem tridimensional, de superfície livre e com o bordo da placa livre para se mover, não é adequado. Pelo menos para o caso em que se considera uma placa com a extremidade livre. O próximo passo a seguir será executar simulações numéricas para o caso em que a placa tem a extremidade fixa de modo a comparar com os resultados laboratoriais aqui obtidos.

Palavras-chave: tectonofísica, subducção, velocidade de afundamento, dinâmica de placas

Contents

List of Figures

List of Tables

1 Introduction

Subduction is an important stage of the plate cycle described by Wilson [1965], in which the kinematic and geodynamic evolution of tectonic plates are summarized in a simple way. Subduction takes place on convergent plate boundaries where one tectonic plate (the subducting plate) sinks into the mantle under another plate (the overriding plate), implying destruction of lithosphere. Although this definition seems simple, the subduction process is very complex. According to many authors the negative buoyancy of a subducting slab, due to plate-mantle density contrast, is the primary driving force for plate tectonics and mantle convection [e.g., Forsyth & Uyeda, 1975; Conrad & Hager, 1999; Bellahsen et al., 2005]. Focusing only on the slab, this force is resisted by viscous bending at the trench and by viscous drag on the slab from the upper mantle [Conrad & Hager, 1999].

Plate subduction kinematics and/or dynamics studies are accomplished using idealized models in which, most often, a single high viscosity analogue plate sinks into an analogue mantle. The only driving force considered is the negative buoyancy due to the plate-mantle density contrast, so they are often referred to as free subduction models, since they model the "free-falling" of the plate into the mantle. Two very common characteristics of these models are 1) the absence of an overriding plate, assuming a weak plate boundary with the same viscosity as the mantle, and 2) the subducting plate is oceanic, to simplify the problematic since the drag on the bottom of the plate which resists the motion is smaller compared to that of continental crust [Forsyth & Uyeda, 1975] and the composition of oceanic crust is far less varied than continental crust reducing the range of some variables.

Several studies have shown that, during the subduction process, the motion of the trailing plate can be accompanied by motion of the trench itself, which as been reported as trench retreat, when the trench moves opposite to the plate motion, or trench advance when the trench moves in the same sense as the plate [Jacoby, 1973; Funiciello et al., 2003b; Schellart, 2008]. This has a major impact the understanding the plates migrations, since the convergent boundaries may not be static and can have varying velocities.

The subduction of a plate induces mantle flow patterns around the slab, as any other body moving trough a fluid more or less would. In the literature one can find studies that show differences on the patterns of slab sinking and consequent mantle flow both in a two-dimensional [e.g., Funiciello et al., 2003a, 2006; Schmeling et al., 2008; Stegman et al., 2006; Ribe, 2010] and a three-dimensional approach [e.g., Funiciello et al., 2003b; Bellahsen et al., 2005; Li & Ribe, 2012; Schellart, 2008], some use analogue laboratory experiments others use numerical investigations, or even both.

Funiciello et al. [2003b] proposed that the mantle flow due to a sinking slab would occur first around the slab tip - poloidal flow - and after slab interaction with a bottom boundary the flow would be around the slab lateral edges - toroidal flow. Funiciello et al. [2006] showed that both return flow oriented around the slab lateral edges and return flow around the slab tip were induced simultaneously in the process. Stegman et al. [2006] refined this idea suggesting that the return flow in a toroidal fashion was the predominant one occurring with an intensity about 3 to 4 times larger then the poloidal flow.

Schellart [2008] and Li & Ribe [2012] also observed a strong toroidal return flow around the slab edges and a two-cell poloidal pattern, in with one cell located under the plate and the other in

the mantle wedge, and they observed no mass transport around the slab tip. They demonstrated that the mantle particles are always in the same poloidal cell, but due to time evolution of the entire system the boundary between the two cells rotates mimicking a return flow around the slab tip. Therefore, a three-dimensional approach to study the mantle convection due to subduction is essential, since in 2-D models the only possibility for a return flow would be in a poloidal fashion around the slab tip.

But because tectonic plates exist in Nature with a wide range of different sizes (length, width and thickness), different density contrasts and different slab-mantle viscosity ratios the style of subduction kinematics may have some differences too. Four major modes of subduction have been identified, Schellart [2008] them described, for narrow plates, as function of slab to mantle viscosity ratio and mantle to plate thickness ratio: mode I is characterized by slab draping geometry, concave trench geometry and trench retreat, mode II by slab folding, draping geometry and episodic trench migration, mode III by slab rollover and trench advance and mode IV by slab draping geometry, rectilinear trench geometry and trench retreat.

Like in most studies, Schellart [2008] did not take into account the existence of an overriding plate, but Duarte et al. [2013] showed that its presence has a major impact on kinematics and dynamics of subduction process, i.e. it also has an impact on the mode of subduction, but this subject is still under investigation.

It is not just the mode of subduction that is variable, trench advance/retreat and sinking velocities can be highly variable too. Ribe [2010] in 2-D and Li & Ribe [2012] in 3-D numerical experiments tested the sinking velocity dependency on plate properties such as plate width, initial slab tip length, initial slab tip dipping angle and mantle depth. They defined a dimensionless parameter to quantify the mechanical resistance of a subducting viscous sheet relative to that of the mantle, the plate *stiffness*. They proposed that the stiffness, the plate width to slab tip length ratio, the mantle depth to slab tip length ratio and the initial slab tip dipping angle control the dynamics of subduction, having a strong influence on plate sinking velocity and on the mode selection. In 3-D it was noticed that the sinking velocity of the slab lateral edges can differ from the sinking velocity of the slab center, causing lateral transverse deformation that has been observed before. The difference between the two sinking velocities can be explained by the fact that the slab lateral borders are affected by a drag from the mantle implying that its velocity does not depend on the plate width, whatever the width is [Li & Ribe, 2012].

Demonstrating the complexity of the subduction process, it has also been shown that it does not evolve as a steady state process [e.g., Funiciello et al., 2003b; Bellahsen et al., 2005], but a three stages sequence after initiation:(1) slab sinking into the upper mantle in a transient way, (2) interaction with a deep viscosity discontinuity and (3) steady state subduction.

To achieve these kind of results, numerical models are often employed using a lubrication layer of low viscosity right above the plate to maintain it in isostatic equilibrium as it is allowed to move freely as response to the pull of the deforming slab, i.e. to prevent the plate from sinking as a whole. But the lubrication layer imposes a free-slip condition that is not very realistic since the subduction process produces topography. Schmeling et al. [2008] compared 2-D models with such a soft layer, models with zero-density weak zone to mimic a free surface and a 3-D laboratory experiment and showed that if a free surface is applied the results are closer to those of the laboratory experiments. They benchmarked 2-D free surface numerical models with laboratory experiments in which the plate used was as wide as the box minimizing the 3-D effects, allowing it

to be considered as a 2-D model too. As it was mentioned before a 2-D approach it is not very accurate to simulate the subduction process.

Numerically, a free surface is challenging to compute because the density contrast that drives the process is a lot smaller than the density contrast between the crust and atmosphere, therefore more sophisticated numerical algorithms that employ larger time steps have been developed to overcome the issue [e.g., Kaus et al., 2010].

In the present study the goals were to investigate the effects of initial slab tip length and initial slab tip dipping angle on the subduction process, specially on the slab tip velocity which allows to infer the plate sinking rate. The subduction process is carefully analysed until the slab reaches the bottom boundary. An attempt to benchmark 3-D free surface numerical models with laboratory experiments is made.

To this end, a combination of laboratory experiments and numerical simulations, in which the initial slab tip length and initial slab tip dipping angle are varied, is used. In first place, the laboratory experiments are presented, a set of three-dimensional models of an entirely dynamically driven but fixed slab was analysed. Then, the numerical simulations are described, the code models plate with a free trailing edge and was benchmarked with the laboratory experiments of Schellart [2008], in particular the experiment hereinafter referred to as DM8, which is a deep mantle model. Both laboratory and numerical experiments model a plate sinking in a whole mantle (i.e. a mantle with no viscosity contrasts at depth) with a free surface and the only driving force is the negative buoyancy of the plate. The subduction initiation was not the focus and temperature and phase changes were not considered.

It shall be shown that plate sinking rate into the mantle depends greatly on the initial slab tip length and less on the initial dipping angle, moreover it also depends if the trailing edge is fixed or free.

2 Methods

2.1 Scalings

In fluid dynamics there are dimensionless numbers that characterize a system. Because it is quite impossible to investigate Earth dynamics within real dimensions models in our lifetime, these numbers allow building analogue models of lithosphere-mantle interactions at reduced time and length scales to reproduce the Earth dynamics. Therefore, the two analogues models used here were scaled to make comparisons with natural systems possible.

The free sinking of a plate can be compared to a rising sphere in a viscous incompressible fluid, in the sense that both movements are driven only by buoyancy. The sphere rises because it is less dense than the ambient fluid and the plate sinks because it is denser. The upward velocity of the sphere is known as the *Stokes Flow* solution ($v_{Stokes} = 2\Delta\rho g a^2/9\eta_{ext}$) [Turcotte & Schubert, 2002], where a is the length scale that characterizes the sphere, i.e., its radius, $\Delta\rho$ is the density contrast that drives the process, g is the gravity acceleration and η_{ext} is the ambient fluid viscosity. The factor $2/9$ is merely geometric.

But this solution for the Stokes flow is defined for a sphere or can be adapted for shapes such as ellipsoids. In here, a plate with more rectilinear shapes is used, with a slab tip of length l, width w and thickness h, so a different approach is used to estimate a characteristic velocity V. Following Li & Ribe [2012], with the focus on the balance of forces acting on the slab tip of initial length l_0 (they use the slab tip length plus a flexural bulge because their slab tip is arcuate, here a bent tip is used) and width w. Assuming negligible bending resistance, the effective buoyancy of the slab tip ($F_b \sim \Delta\rho g h l_0 w$) is approximately equal to the traction applied to the bending portion by the outer fluid integrated over the slab tip area ($F_{ext} \sim \eta_{ext} V w$) resulting in

$$V \sim \frac{\Delta\rho g h l_0}{\eta_{ext}} \equiv v_{Stokes} \tag{1}$$

The Stokes solution is only valid if the Reynolds number, $Re = \rho v_{Stokes} l_0/\eta$, which compares inertial forces with viscous forces, is less than 1, to ensure that the flow is laminar and controlled by viscous forces. Note that l_0 was used as the length scale.

A characteristic time t^* was also estimated, considering it as the time that the slab tip takes to reach the bottom of a mantle with a total depth of H sinking at the v_{Stokes} velocity, as

$$t^* \simeq \frac{H}{v_{Stokes}} \tag{2}$$

The analogue plate and mantle dimensions and their rheological parameters for both numerical and laboratory models are summarized on Table 1. The two models are described in more detail in the next subsections.

A deep mantle with no discontinuities was assumed with a thickness of 2280 km, the same natural value used by Schellart [2008]. The Nature-model length scale ratios for both models were set to correspond this assumption: the laboratory mantle was 45 cm thick and the numerical mantle was 38 cm , so 1 cm corresponds to 50 km in Nature for the laboratory model and 60 km for the numerical model.

Table 1. Laboratory and numerical models and of DM8 experiment parameters. Values for an ideal Nature system are also shown for reference. Models configurations for the laboratory and numerical experiments are depicted on Figures 1 and 2, respectively.

Parameter	Laboratory	Numeric	DM8	Nature[i]
Gravity acceleration, m/s^2	9.8	9.8	9.8	9.8
Length, m				
L, mantle	1	1	1	
Thickness, m				
H, mantle	0.45	0.38	0.38	2280×10^3
h, plate	0.01	0.013	0.013	78×10^3
Width, m				
W, mantle	0.60	0.60	0.60	3600×10^3
w, plate	0.2	0.15	0.15	900×10^3
Density, kg/m^3				
ρ_m, mantle	1414	1420	≈ 1417	3200
ρ_p, plate	1513	1500	≈ 1500	3300
$\Delta\rho$	99	80	80	100
Viscosity, Pa·s				
η_m, mantle	100	100	100	10^{21}
η_p, plate	64000	25250	25250	10^{22}
$\gamma = \eta_p/\eta_m$	640	252.5	253	10^2

On table 2 the different initial parameters (l_0 and θ_0) tested are displayed for all the laboratory and numerical experiments, including the DM8 experiment. The Stokes velocity, characteristic time and Reynolds number are also summarized. Because the Reynolds number is very low in every case, it is valid to use the v_{Stokes} and characteristic time calculated for all experiments, which will be referred to as the theoretical values, to be compare with the velocity results from the experimental data.

Table 2. Stokes velocity, characteristic time and Reynolds number for all experiments.

	l_0 [m]	θ_0 [°]	v_{Stokes} [m/s]	t^* [s]	Re
Lab-1	5.2×10^{-2}	≈ 16	5.07×10^{-3}	88.7	2.63×10^{-4}
Lab-2	4.3×10^{-2}	≈ 20	4.20×10^{-3}	107	1.80×10^{-4}
Lab-3	2.3×10^{-2}	≈ 24	2.27×10^{-3}	198	5.28×10^{-5}
Num-1	2.5×10^{-2}	60	2.55×10^{-3}	149	5.10×10^{-5}
Num-2	2.5×10^{-2}	90			
Num-3	3.3×10^{-2}	30	3.36×10^{-3}	113	8.88×10^{-5}
Num-4	3.3×10^{-2}	60			
Num-5	5×10^{-2}	26	5.10×10^{-3}	74.6	2.04×10^{-4}
Num-6	6×10^{-2}	26	6.12×10^{-3}	62.1	2.94×10^{-4}
DM-8	3.19×10^{-2}	≈ 30	3.25×10^{-3}	117	1.91×10^{-5}

[i]Nature length values presented were calculated assuming the model-Nature length ratio of 6×10^6 and using the DM8 experiment as reference.

Analogue model time scale, t_n/t_m, was obtained calculating the corresponding v_{Stokes} in Nature units for every experiment, combining (1) and (2) and applying (4) to Nature and to each model, where the subscripts 'n' and 'm' refer to Nature and model values, respectively.

$$v_{Stokes} = \frac{\Delta\rho g h l_0}{\eta_{ext}} = \frac{H}{t} \tag{3}$$

$$\frac{t_n}{t_m} = \frac{H_n}{H_m}\frac{h_m l_{0_m}}{h_n l_{0_n}}\frac{\Delta\rho_m}{\Delta\rho_n}\frac{g_m}{g_n}\frac{\eta_{ext_n}}{\eta_{ext_m}} \tag{4}$$

It results that 1 s in the laboratory model represents about $42\,000$ years in Nature and 1 s in the numerical model represents about $62\,000$ years. The DM8 experiment has the same model parameters as the analogue numerical model used, so the length and time scales are the same as the latter.

To check the dependence of experimental velocity results with the initial parameters, l_0 and θ_0, a definition proposed by [Ribe, 2010] and Li & Ribe [2012] was used. The ratio of the internal and external viscous forces acting on bending portion of the plate defines a measure for the 'stiffness' of a subducting plate.

$$\frac{F_{int}}{F_{ext}} \sim \gamma \left(\frac{h}{l_0}\right)^3 \equiv S \tag{5}$$

The dimensionless quantity S defines if the sinking speed is controlled by mantle viscosity (if $S \leq 1$) or by the viscosity of the sheet (if $S \gg 1$). Because they use an arcuate slab tip that corresponds to the slab tip length used in this work plus a flexural bulge, as mentioned before, the tip length they use is longer than the one used here. Nonetheless, the stiffness was calculated using the initial tip length considered in this work.

Still according to Li & Ribe [2012], the sinking velocity of the center of the slab tip, v_s, and Stokes velocity ratio depends on the stiffness, the initial dipping angle, the slab width to initial tip length ratio and on the mantle thickness to initial slab tip length ratio (6). This last ratio is included because the presence of a boundary at depth has been shown to have impact on v_s/v_{Stokes} ratio [Li & Ribe, 2012], in this work the mantle thickness is not varied but the initial slab tip length is, so the ratio varies. They tested this dependency on numerical models with a lubrication layer, here, it is investigated using free-surface models. Again, the l used is not the same as in Li & Ribe [2012].

$$\frac{v_s}{v_{Stokes}} = fct\left(S, \theta_0, \frac{w}{l_0}, \frac{H}{l_0}\right) \tag{6}$$

The analysis of this functional shall be discussed in section 4.2.

2.2 Laboratory Experiments

Three experiments (setup on Figure 1) were carried out using a plate made of high-viscosity linear viscous silicone (Rhodorsil Gum FB) mixed with iron powder of thickness h as a plate fixed on one side, with a slab tip of length l_0 and a trailing plate of length L_p, to model an oceanic plate. The different initial parameters, l_0 and θ_0, were forced manually. The viscosity of the plate is η_p and the density ρ_p. A viscous rheology for the lithosphere is an adequate first order approximation since, at geological time-scales, a subducting plate acts like some kind of fluid [Houseman & Gubbins, 1997].The plate was set to sink into an analogue deep mantle composed by a glucose syrup of viscosity η_m and density ρ_m. The values of the mentioned parameters are listed on Tables 1 and 2.

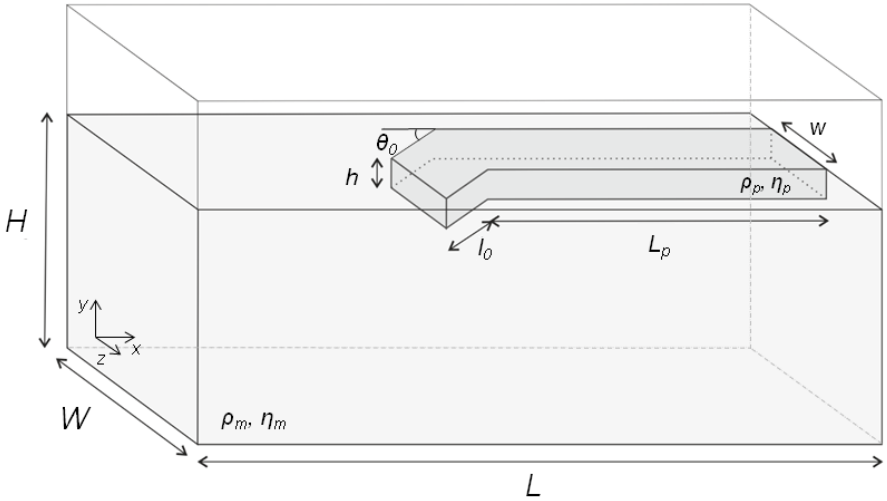

Figure 1. Configuration of the laboratory experiments. A silicone putty mixed with iron powder of thickness h represents a plate fixed along its trailing edge to one of the lateral walls. Its tip is bent over a of length l_0 and the trailing plate has the length L_p. The viscosity of the plate is η_p and the density ρ_p. Representing the mantle is a glucose syrup of viscosity η_m and density ρ_m. The analogue mantle has a total height of H, width W and length L. Three experiments were carried out using different initial slab tip lengths and dipping angles. Free subduction is driven only by gravity forces due to the mantle-plate density contrast.

Two cameras were used to record the experiments taking pictures every 10 s, one from a side view and the other from a top view of the box. Considering the three dimensional Cartesian coordinate system, the opposite wall where the plate is fixed was defined as $x = 0$ m, the bottom boundary as $y = 0$ m and the back wall as $z = 0$ m. The pictures were taken from a side perspective containing the plane $z = 0.6$ m and from a top view containing the plane $y = 0.45$ m.

Using a picture analysing software, several measurements were made from every picture for the three laboratory experiments: (a) the depth of the slab tip - distance between the most deep visible slab point at $z = 0.6$ m plane and the bottom, (b) the depth of the slab lateral edge tip - distance between the closest point of the slab to boundary $z = 0.6$ m and the bottom, (c) the trench displacement - distance between the point where the center of the slab width starts to be submersed and the boundary $x = 0$ m, (d) the initial slab tip length, and (e) the initial slab tip dipping angle.

Two different measurements of the slab tip vertical position were taken because the center of the slab, for all the experiments, tended to be deeper than the plate lateral borders after the first moments.

It is important to keep in mind that the laboratory conditions, despite all efforts, may vary and, for as little as those variations may be, they can influence the results. Due to small changes in the ambient fluid temperature caused by changes on room temperature itself, the analogue mantle viscosity is not exactly the same between experiments. A temperature change, for as small as it may be, could influence the fluid viscosity [Schellart, 2011]. Therefore, the relevance of this influence is investigated on the Stokes velocity (1).

The relation between the viscosity of a fluid and its temperature follows the Arrhenius equation (7). Using this relation on (1) one obtains (8), where η_0 is a reference value (2.41×10^{-16} Pa·s [Schellart, 2011]), R is the noble gas constant (8.314472 J·K^{-1}·mol^{-1}) and E is the energy activation (100.79 kJ·mol^{-1} [Schellart, 2011]), to keep the units coherent on the equation, the temperature values used have to be converted to kelvin degrees . The values of η_0 and E used were chosen from Schellart [2011] to better correspond to the fluid density used here.

Thus is possible to check the Stokes velocity dependency on the temperature of the medium, and it is expected that an increase in the medium temperature implies a decrease on its viscosity, which should lead to an increase on the sinking velocity.

$$\eta(T) = \eta_0 e^{\frac{E}{RT}} \tag{7}$$

$$v_{Stokes}(T) = \frac{\Delta\rho g h l_0}{\eta_0 e^{\frac{E}{RT}}} \tag{8}$$

2.3 Numerical Model

The numerical simulations were obtained with a code that uses a mixing of the finite element method (FEM) with the maker-and-cell method [May et al., 2014]. It is assumed an incompressible fluid with infinite Prandtl number, which implies low Reynolds number, in a three-dimensional Carthesian geometry, which means that the fluid diffuses momentum more rapidly than heat and the viscous effects dominate over inertial effects. There is no inertial term therefore the problem is reduced to

$$\nabla \cdot \mathbf{v} = 0 \tag{9}$$

$$\Delta\rho\mathbf{g} - \nabla P + \nabla \cdot [\eta(\nabla\mathbf{v} + (\nabla\mathbf{v})^T)] = 0 \tag{10}$$

where P is the dynamic pressure, $\Delta\rho$ is the density contrast, $\mathbf{g}$ is the gravity acceleration vector, $\mathbf{v}$ is the velocity vector and η is the dynamic viscosity of the fluid.

In Figure 2 the initial setup for the numerical model is shown, but only half ($z < 0.3$ m) of the total domain is displayed for better viewing, although the numerical experiments were performed

in the whole domain. The Cartesian coordinate system is also depicted, its origin is the corner between the left, back and bottom walls, similarly to that of the laboratory setup.

A sheet representing a lithospheric plate of density ρ_p, higher than the density of the mantle ρ_m, and high viscosity η_p rests on top of the mantle of viscosity η_m with, on one end, a tip of length l_0 with the same plate density and viscosity, dipping into the mantle with an initial angle θ_0, between the mid-surface of the slab tip and the top surface of the mantle. On the other end, the plate is free to move trenchwards as the subduction process evolves,initial the edge is 14 cm away from the right wall. The values of the mentioned parameters are listed on Tables 1 and 2.

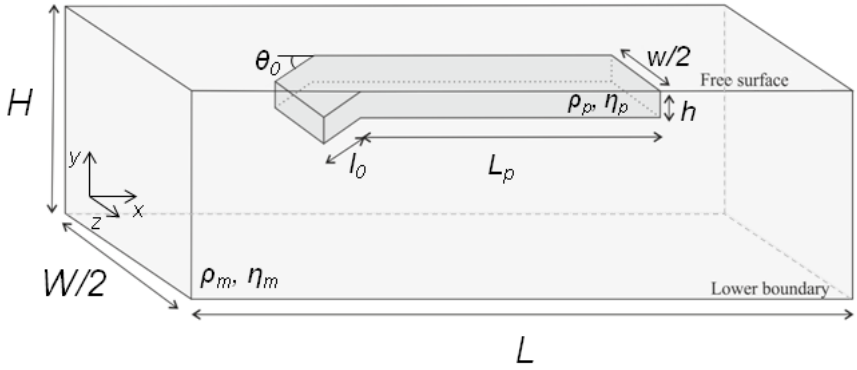

Figure 2. Configuration of the numerical model. Only half of the domain is shown ($z < 0.3$ m), although the simulations were performed in the entire domain. A plate of density ρ_p and viscosity η_p rests on top of the mantle of density ρ_m and viscosity η_m. A tip of length l_0 with the same plate density and viscosity is initially dipping into the mantle with an angle θ_0, between the mid-surface of the tip and the top surface of the mantle. The other end of the plate is free to move trenchwards. Free subduction is driven only by gravity forces due to the mantle-plate density contrast.

The mantle is uniform and limited at all its boundaries by rigid no-slip surfaces, except on top where free-surface is assumed and the bottom boundary represents the mantle-core discontinuity.

Different values for the initial slab tip length and dipping angle were tested (values listed on Table 2) and for every experiment the minimum vertical position - y_{min} - of the slab tip, trench and trailing edge positions were registered in time.

3 Results

The time evolution of the slab shape, slab tip position and trench motion are described first for the laboratory experiments and then for the numerical simulations. The DM8 experiment is always shown with the numerical experiments results. Comparisons are made in section 4.

3.1 Laboratory Experiments

3.1.1 Sinking evolution

The laboratory experiments, despite the differences in initial slab tip length and dip angle (experiment parameters are defined on Tables 1 and 2 and the model setup is depicted on Figure 1), show roughly the same behaviour as the plate sinks (see Figures 3 and 4). The experiments differ on the time interval in which the system evolves, therefore only the fastest and the slowest experiments, Lab-1 and Lab-3, respectively, are shown. The Lab-2 evolution is very similar to Lab-1.

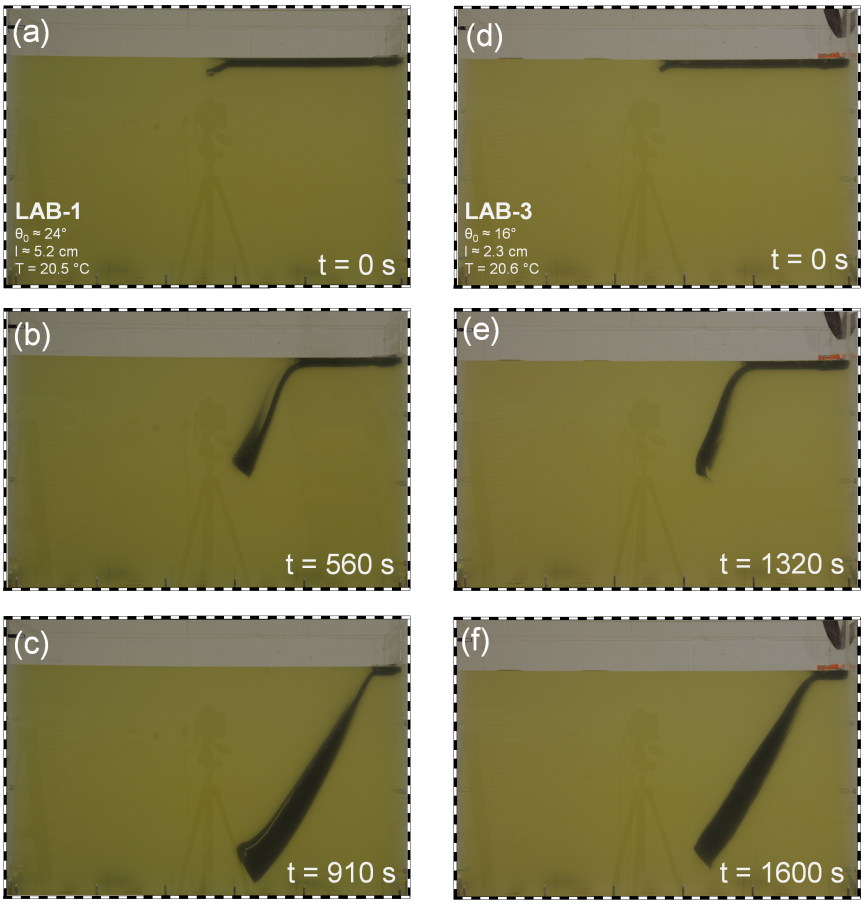

Figure 3. Laboratory side-view experiments photographs. The evolution of the slab is shown at three different moments in time: the first and last moments and one middle stage when the tip reaches $y = 20$ cm. Note that the pictures were taken from the $z = 0.60$ m perspective and the center of the plate is at $z = 0.30$ m, meaning that there is a corrective length factor between the box wall and the actual position of the plate. (a-c) Experiment Lab-1 at time $t = 0$, 560 and 910 s, and (d-e) Experiment Lab-3 at time $t = 0$, 1320 and 1600 s.

On Figures 3 and 4 three moments int time are presented: the first moment, the stage when the slab tip reaches the $y = 0.2$ m plane and the moment when the tip reaches the bottom boundary. Initially the dipping angle of the slab tip increases until it is sub-vertical, decreasing slightly afterwards and maintaining until the bottom boundary is reached. Between Figures 3b and 3c, for Lab-1, and 3e and 3f, for Lab-3, one can see that the angle between the slab and the surface has decreased a little. A difference in plate geometry is visible between Figure 3b and 3e, the lateral border of the slab on experiment Lab-1 acquires a more curvilinear shape and its tip points towards the mantle wedge. On Lab-3, the tip of the slab points in the opposite direction.

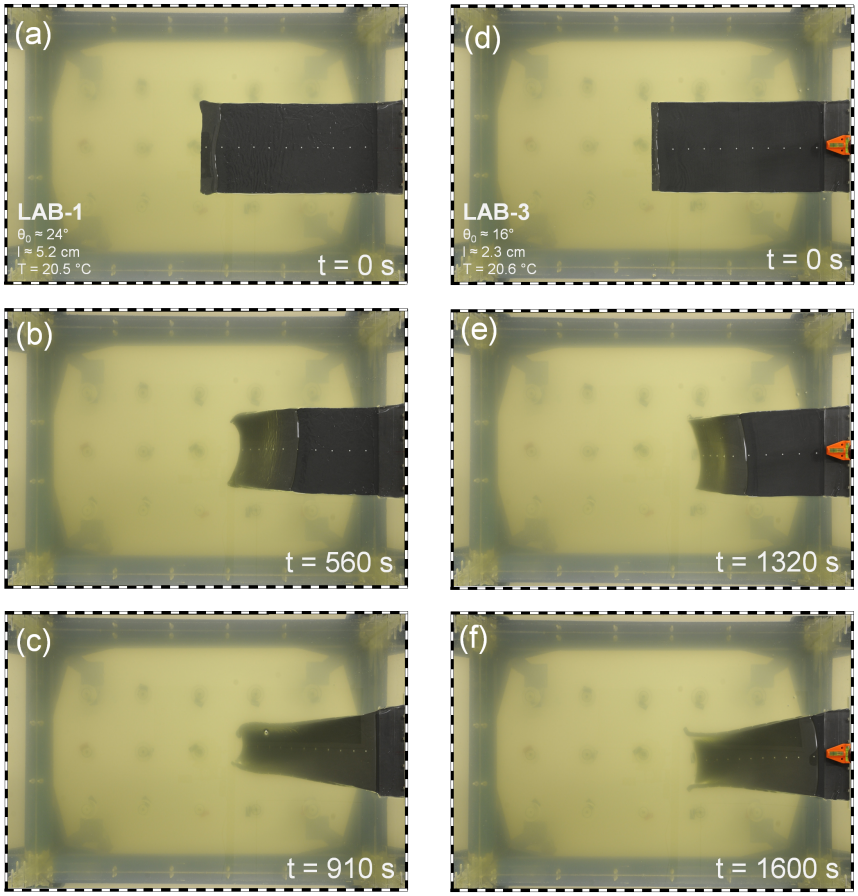

Figure 4. Laboratory top-view experiments photographs. The evolution of the slab is shown at three different moments in time: the first and last moments and one middle stage (when the tip reaches $y = 20$ cm). Note that the pictures were taken from the $z = 0.60$ m perspective and the center of the plate is at $z = 0.30$ m, meaning that there is a corrective length factor between the box limits and the actual position of the plate. (a-c) Experiment Lab-1 at time $t = 0$, 560 and 910 s, and (d-e) Experiment Lab-3 at time $t = 0$, 1320 and 1600 s.

From a top-view, comparing Figure 4c and 4f, experiment Lab-1, which has the longest initial slab tip length and the the lowest dipping angle, exhibits the most concave slab geometry and experiment Lab-3, which has the smallest l_0 and highest θ_0, takes the longest to reach the bottom. The differences in the slab geometry should be attributed to the different initial conditions that implicate different sinking velocities (as it is theorized on Table 2).

In these experiments, the trailing edge of the plate was fixed, as a result, the subduction was mostly accommodated by trench retreat, and to a smaller degree by trenchward subducting plate

motion, restraining the mode of subduction.. A description of the mantle flow is not possible because there were no tracers inside the mantle, so the focus is on the different motions measurable.

3.1.2 Plate and trench motion

Figure 5 compares the center and the lateral border of the slab tip vertical position for each experiment. All experiments show very similar pattern behaviours. As expected looking to the concave shape of the slab, the slab border is always at little higher vertical position since the border suffers the most effects of drag by the mantle.

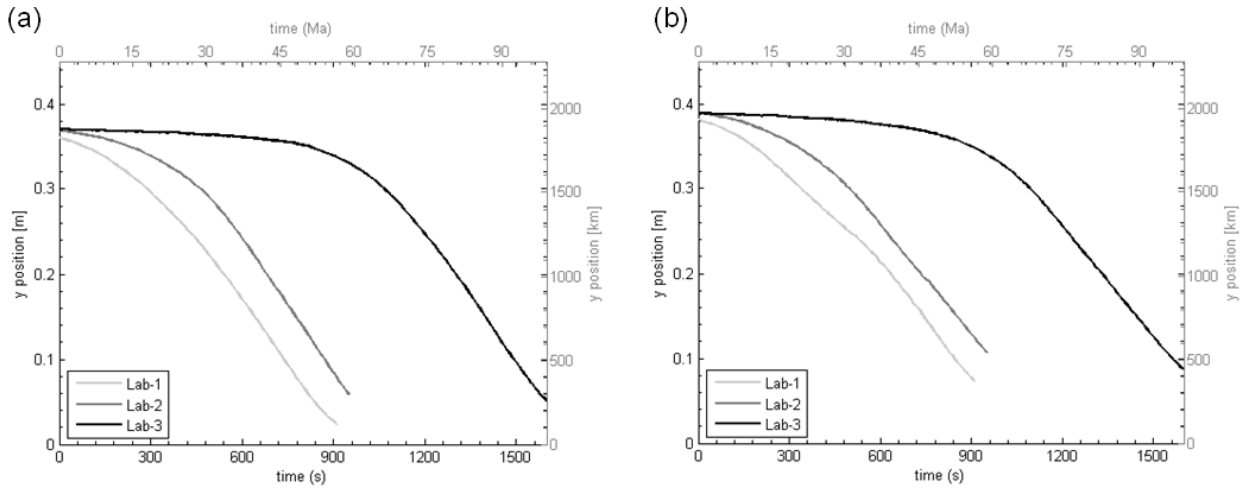

Figure 5. Laboratory experiments time evolution of the slab tip position at (a) the center and (b) lateral border. The curves follow the deepest point of the slab, the y-axis corresponds to height of the slab tip relative to the bottom of the box on plane $y = 0$ m. Model and Nature dimensions are represented.

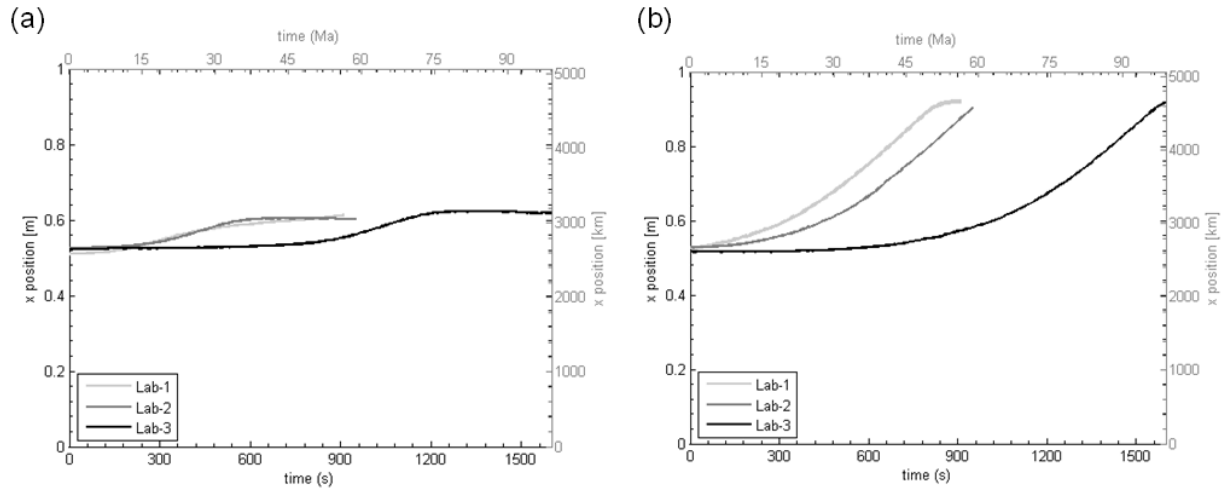

Figure 6. Laboratory experiments time evolution of (a) the horizontal displacement of the center of the slab tip and (b) the trench motion. The y-axis represents the displacement of the slab tip relative box wall at $x = 0$ m. Model and Nature dimensions are represented.

The total horizontal displacement of the slab tip border, presented on Figure 6a, is similar to all experiments but the time intervals in which the tip moves more significantly varies, specially for the Lab-3 case.

Looking to Figure 5, the Lab-3 experiment takes much longer to start sinking significantly, this experiment has the smallest initial slab tip length, so one explanation could be that the system has to develop a critical slab tip to evolve, i.e. the tip has to reach a certain depth or the dip angle has to increase to a critical value.

3.1.3 Slab sinking and trench velocities

In this work, the focus is the evolution of the slab until the bottom boundary is reached, which has been described in the literature as the transient state [e.g., Funiciello et al., 2003b; Bellahsen et al., 2005]. With the obtained results, it is possible to see that this state can also be described as a sequence of stages. In Figure 5, after an initial transient state, during which the evolution of the slab tip position varies depending on the initial conditions, the system evolves in a steady state until the bottom is reached. The trench displacement also shows this type of pattern (Figure 6b) at the same time interval but the border tip horizontal displacement (Figure 6a) has a linear growth on a earlier time interval, staying almost at a constant position during the identified steady state for the center of the slab tip position on Figure 5.

Therefore, it is possible to estimate slab tip sinking (both at the center and at the border) and trench retreat velocities by linear fitting. The calculated slopes should correspond to the slab tip sinking velocity at its center, v_s, at its border, v_b, and to trench retreat velocity, v_t, for each experiment, since they represent a space derivative in time. A horizontal velocity for the border of the slab tip was not estimated, it is not considered to be relevant for this study.

The results are summarized on Table 3 as well as the coefficients of determination. The intervals on which the linear fittings were made are on Table 4. All different fittings for the same experiment were accomplished using in the same time interval, since all curves show linearity on that interval. Note that the velocities absolute values are shown to simplify, because the directions do not vary between experiments: sinking velocities are always towards the bottom and trench always moves in the direction of the plane $x = 1$ m.

The sinking velocities of the center and border of the slab tip and the trench velocity vary very little between experiments. The slab tip border has a smaller velocity than the center tip, as it was expected due to the geometry the slab developed throughout the experiments. The center of the slab sinks faster than the sides because is less affected by lateral drag from the mantle [Li & Ribe, 2012]. The trench velocity, in turn, has higher values than the sinking velocity, which could explain the decrease on the slab dip noted at the last moments of the experiment (Figures 3c and 3f).

To From Table 3, the maximum change in velocities is noted between experiments Lab-1 and Lab-2. The center of the slab tip sinking velocity decreases 2.5%, the slab tip border sinking velocity decreases 5.8% and the trench velocity decreases 3.3% in response to a change in the initial slab tip length of 21% and a change in theta of 25%.

One important result is that for a fixed plate, the sinking velocity does not change significantly with changing initial conditions, still only three experiments were carried out.

Table 3. Laboratory experiments sinking and trench motion velocities. Model and Nature units are summarized. The initial values of l_0 and θ_0 are on Table 2.

	Slab center tip			Slab Border tip			Trench		
	$\lvert v_s \rvert$ [m/s]	$\lvert v_s \rvert$ [km/Ma]	r^2	$\lvert v_b \rvert$ [m/s]	$\lvert v_b \rvert$ [km/Ma]	r^2	$\lvert v_t \rvert$ [m/s]	$\lvert v_t \rvert$ [km/Ma]	r^2
Lab-1	5.13×10^{-4}	42.00	0.9998	4.54×10^{-4}	37.15	0.9978	6.95×10^{-4}	56.90	0.9995
Lab-2	5.26×10^{-4}	43.06	0.9999	4.29×10^{-4}	35.08	0.9997	6.72×10^{-4}	54.97	0.9992
Lab-3	5.17×10^{-4}	42.30	0.9996	4.32×10^{-4}	35.33	0.9999	6.52×10^{-4}	53.34	0.9989

Table 4. Linear intervals of the laboratory experiments. The time, the slab tip center and lateral edge y positions and the trench x position are shown in both model and Nature units. The subscripts 'i' and 'f' represent the beginning and the end of the interval considered linear, respectively.

	Model units								Nature units							
			Slab center tip		Slab border tip		Trench				Slab center tip		Slab border tip		Trench	
	t_i [s]	t_f [s]	y_i [m]	y_f [m]	y_i [m]	y_f [m]	x_i [m]	x_f [m]	t_i [Ma]	t_f [Ma]	y_i [km]	y_f [km]	y_i [km]	y_f [km]	x_i [km]	x_f [km]
Lab-1	540	830	0.200	0.053	0.236	0.106	0.710	0.905	33.4	51.4	1013.0	269.8	1197.9	536.4	3599.5	4586.6
Lab-2	570	950	0.257	0.059	0.271	0.107	0.649	0.902	35.3	58.8	1301.3	297.3	1374.3	541.4	3288.9	4569.3
Lab-3	1240	1570	0.230	0.063	0.238	0.097	0.693	0.904	76.8	97.2	1163.8	317.9	1205.5	489.4	3510.1	4582.4

3.1.4 Mantle viscosity

The analogue mantle temperature for every experiment was measured, in Lab-1 and Lab-2 it was registered a temperature of 20.5 ° C and in Lab-3 a temperature of $T = 20.6$ ° C. The impact of a small temperature unwanted change in the mantle fluid is examined using the relation (8).

Table 5. Stokes velocity dependency on the ambient fluid temperature.

Experiment	T [° C]	$\eta(T)$ [Pa·s]	v_{Stokes} [m/s]	$v_{Stokes}(T)$ [m/s]
Lab-1	20.5	204.28	5.1×10^{-3}	2.5×10^{-3}
Lab-2	20.5	204.28	4.2×10^{-3}	2.1×10^{-3}
Lab-3	20.6	201.43	2.3×10^{-3}	1.1×10^{-3}
reference[ii]	25.67	100	2.3×10^{-3}	2.3×10^{-3}

A comparison between the calculated Stokes velocity (Table 2) and the temperature dependent Stokes velocity is made on Table 5 for the three experiments. A reference value for $v_{Stokes}(T)$ was calculated as well because the temperature measured imply smaller mantle viscosity than was intended for the analogue model so a theoretical value was calculated assuming the temperature to which the desired mantle viscosity (100 Pa·s) results. The Stokes velocity for this reference setting was calculated using a initial tip length of 2.3 cm (the smallest length used on the laboratory experiments).

The highest variation on v_{Stokes} is between experiments Lab-1 and Lab-3, a decrease of 54.9% is observed. The variation of $v_{Stokes}(T)$ between this two experiments is 56%, which is not very different. Because the experiments are laboratory they are more prone to have higher errors associated, so it is safe to assume that the temperature did not affect the plate sinking rate significantly.

3.2 Numerical Experiments

3.2.1 Sinking evolution

The numerical simulations show little differences as the slab sinks into the mantle, there are mainly variations in the time duration for each experiment, therefore only pictures of two cases are shown: experiment Num-1, which has the lowest initial length tip, and Num-6, which has the highest l_0 (Figure 7). The velocity field and plate shape are shown for four different instants, the first corresponding to the instant $t = 50$ s and other three to the moments when tip reaches the y planes of 32, 20 and 2 cm.

In Figure 7 is visible that, at the beginning, as the slab sinks, the angle between the tip and the surface increases until about $90°$, maintaining until the bottom boundary is reached. On Num-1 experiment, the slab starts with a higher θ_0 so the moment when the rotation stops happens closer to the surface. On the other hand, because l_0 is smaller, this moment takes longer to occur.

[ii] reference is taken as the setup for $\eta_m = 100$ Pa·s, which means that the reference temperature was calculated.

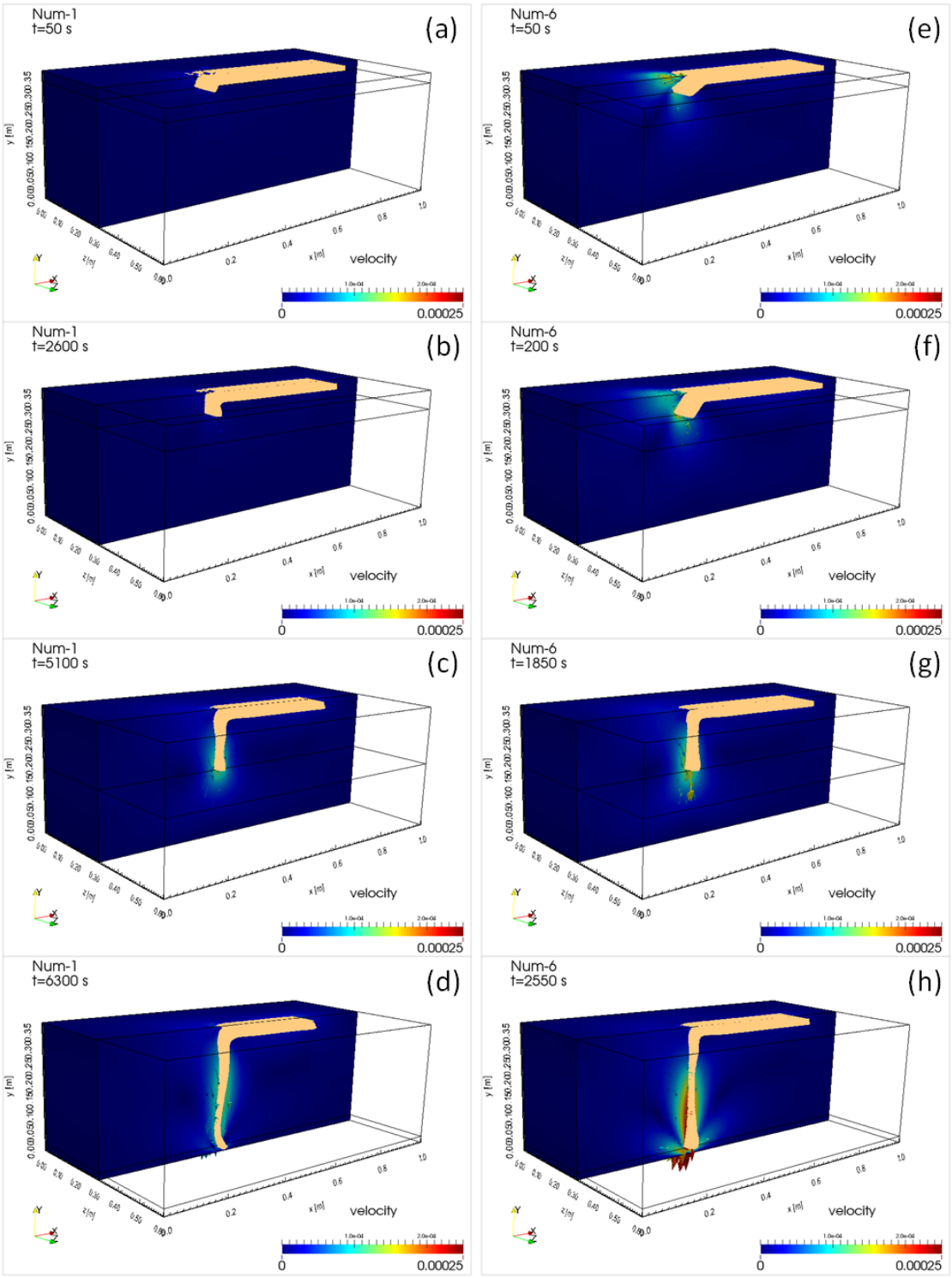

Figure 7. Evolution of slab sinking for numerical experiments (a-d) Num-1 experiment with $l_0 = 2.5$ cm and $\theta_0 = 60°$and (e-h) Num-6 experiment, with $l_0 = 6$ cm and $\theta_0 = 26°$. Four different moments in time are displayed for both experiments: the beginning and the moments when the slab tip reaches the $y = 32$ cm, $y = 20$ cm and $y = 2$ cm planes.

A slab with a higher θ_0 should start sinking freely sooner, but what is noted is that the influence of the initial angle is small compared to that of the initial tip length. Experiment Num-6 (Figure 3(e-h)), which has a higher initial slab tip length shows a more intensified velocity field. So the system evolves quicker because the instability is higher. Taking into account the theoretical values for the sinking velocity (Table 2), this was expected. This results suggest that plates with small initial length tips take longer to start sinking freely.

Besides the obvious differences in the first moment due to the initial geometry of the slab tip, the main difference in the plate shape is noted at the final stages (Figure 7d and 7h) when the slab reaches the bottom: on Num-1 the tip folds in the mantle wedge direction and on Num-6 it bends on the opposite direction.

All experiments show trench retreat and trailing edge motion, concave trench geometry and it is not clear if the slab acquires a draping and folding geometry, but what happens after the slab reaches the bottom boundary is outside this work's objectives.

According to the subduction mode classification of Schellart [2008] this numerical models follow mode I, with trench retreat and concave trench geometry. On Figure 8 the regime boundaries defined, as function of the ratios η_p/η_m and H/h, by Schellart [2008] and the numerical simulations of Li & Ribe [2012] are depicted, as well as the numeric setting used for this study and the DM8 experiment. These boundaries were defined for narrow slabs with ratios between plate width and mantle thickness of $0.4 - 2.7$, in this work this ratio is 0.4, so the comparisons are allowed. As the numerical simulations of this work were benchmarked with the DM8 experiment it is only natural that this two points overlap.

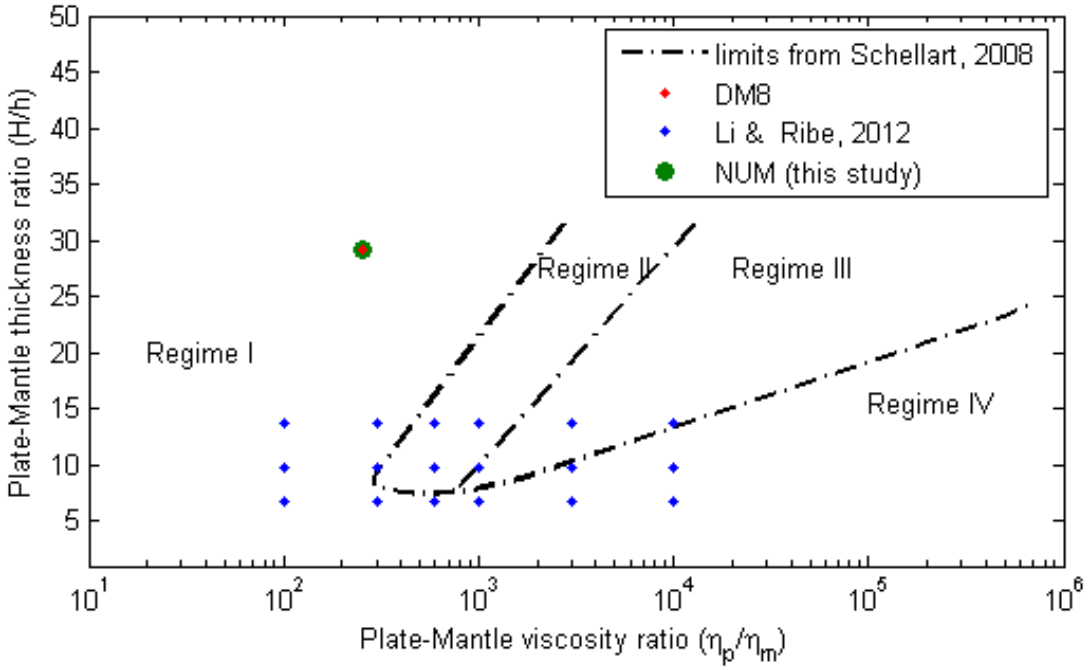

Figure 8. Regime diagram for the laboratory and numerical models, according to Schellart [2008]. The numerical simulations of this study and the DM8 experiment are presented. The Li & Ribe [2012] experiments are also depicted.

3.2.2 Mantle flow

The instantaneous mantle flow for experiment Num-1, at $t = 2600$ s, is illustrated in Figure 9. The subduction induced mantle flow has the same patterns for all experiments, then only example is presented. The patterns found on the mantle flow correspond to what was reported by Li & Ribe [2012] and Schellart [2008]. The arrows representing the flow are not scaled with the mantle velocity field because the its magnitude close to the slab is much higher than at any other point, which means for scaled arrows the velocity vectors not visible away from the slab.

It is visible a toroidal flow around the slab lateral edges in an horizontal section at $y = 0.32$ m and a two poloidal cell system in a cross section at $z = 0.3$ m. Note that in Figure 9a only a cross section of the slab is represented and the the picture represents a top-view of the box. The total box length is not depicted because the flow induced by trailing edge motion its not relevant here.

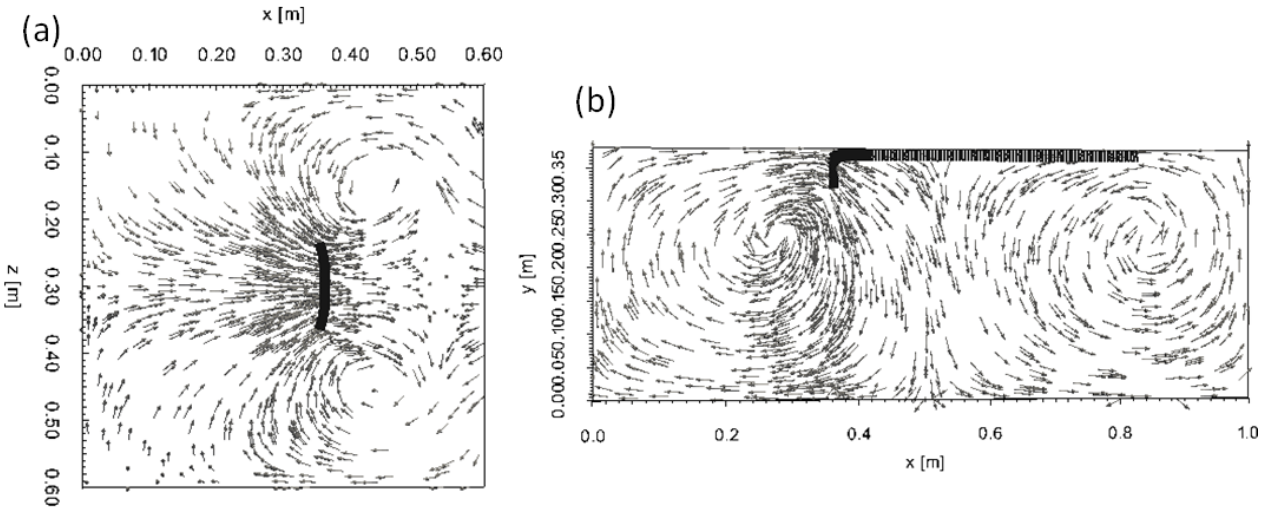

Figure 9. Instantaneous mantle flow illustration for Num-1 at $t = 2600$ s. (a) Toroidal pattern from a top-view at $y = 0.32$ m and (b) poloidal pattern, side view at $z = 0.3$ m. The arrows are not scaled with the mantle velocity field.

3.2.3 Plate and trench motion

In Figure 10 the slab tip position evolution in y direction is displayed for all numerical simulations and for the DM8 experiment. Similarly to what was noticed on the laboratory experiments, all curves show, after an initial transient stage, a phase where the depth increases almost linearly with time, even on the DM8 experiment, which evolves quicker that the numerical simulations.

All experiments show similar behaviour, except Num-5 and Num-6 which show an initial steep stage before the transient stage, that could be due to the fact that when the tip is rotating at the beginning a longer slab tip reaches a deeper position sooner and because the initial dipping angle in this experiments is smaller so the tip rotates more to reach the sub-vertical angle described before (Figure 7(e-h)).

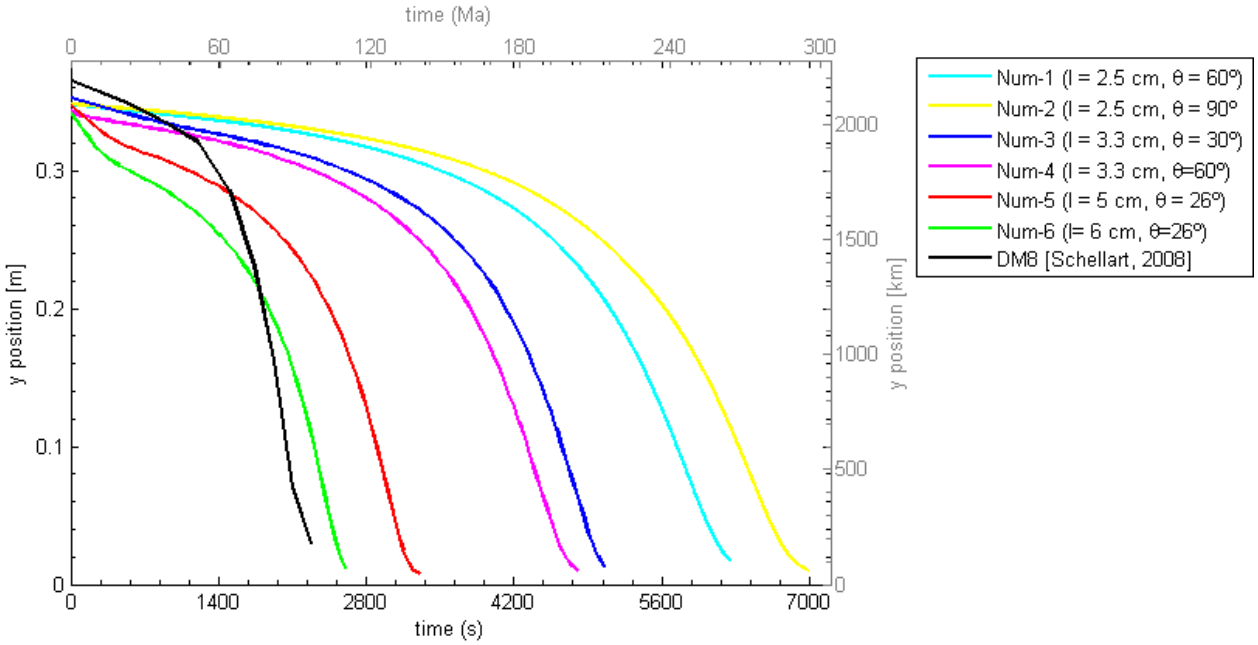

Figure 10. Numerical experiments time evolution of the slab sinking, the curves follow the deepest point of the slab, the y-axis corresponds to the height of the slab tip relative to the bottom of the box on plane $y = 0$ m. Model and Nature dimensions are represented.

It is also visible that for higher l_0 the linear stage starts earlier, meaning that systems with a longer initial slab tip length evolves more rapidly.

Between experiments with the same initial slab tip angle, the impact of an increase of θ_0 is not very pronounced. Between Num-1 and Num-2 the initial angle increases 50% and between Num-3 and Num-4 the angle doubles, but in the first case the start of the steady state is delayed for the higher angle and in the second case it is anticipated, this difference is address again ahead.

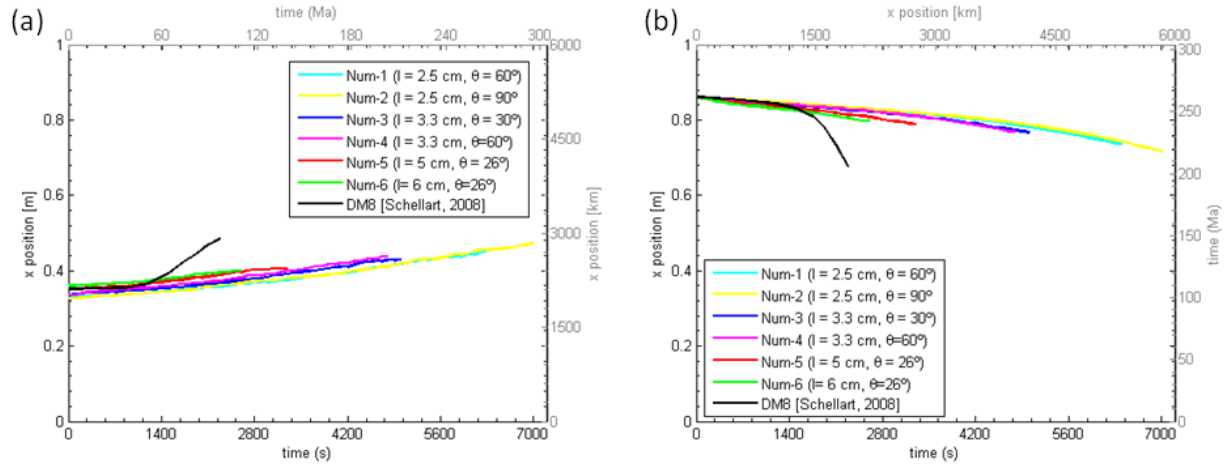

Figure 11. Numerical evolution time evolution of (a) the trench retreat and (b) the trailing edge motion, the y-axis corresponds to displacement of the slab tip relative to the box wall on plane $x = 0$ m.

The trench and the trailing edge positions in x in time are displayed on Figure 11. All curves

are very similar between all experiments for both trench and trailing edge motions, again the main difference is the time interval. The DM8 experiment is the exception, the curves show very different slopes.

The Num-6 experiment exhibits less total trailing edge displacement, suggesting that the plate stretches more during the process.

3.2.4 Sinking, trench and trailing edge velocities

The same linear fitting approach used on the laboratory data was used to estimate sinking, trench and trailing edge velocities. The results are summarized on Table 6 as well as the coefficients of determination. The intervals on which the linear fittings were made are on Table 7. All different fittings for the same experiment were accomplished using in the same time interval, since all curves show linearity on that interval. Again, to simplify, the velocities absolute values are listed.

The maximum sinking and trench velocities registered by Schellart [2008] for the DM8 experimental are 3.26×10^{-4} and 1.35×10^{-4}, respectively. This values were registered when the slab tip was getting closer to the bottom boundary. The values estimated here are very close to these, which means that the linear approach used is reliable.

Experiment Num-3 is the closest numerical setting to the DM8 experiment, but comparing the obtained velocities for these cases it visible that the results do not match. The sinking velocity is lower and the trench and trailing edge velocities are higher in the Num-3 case. Both models have a free surface and a free trailing edge, thus one explanation for the noted difference could be the fact that DM8 is a laboratory model and there could be laboratory effects that are not modelled.

Comparing Num-1 and Num-2 experiments, which have the same l_0, it is clear that the sinking velocity for is lower for Num-2. So, the fact that the steady state on Num-2 starts later (Table 7) could be due to the angle already being at $90°$and the tip does not rotates initially as it starts sinking, on all other cases as the tip rotates and sinks simultaneously.

Observing Table 6, for the same initial slab dip angle, experiments Num-1 and Num-4 ($\theta_0 = 60$ °) and experiments Num-5 and Num-6 ($\theta_0 = 26$ °) an increase 32% and 20% in l_0 results in an increase of 21.6% and 13.4% on the sinking velocity, respectively. This direct influence of l_0 was expected theoretically (Table 2). On the other hand, one notices that for the same initial slab tip length, experiments Num-1 and Num-2 ($l_0 = 2.5$ cm) and experiments Num-3 and Num-4 ($l_0 = 3.3$ cm), an increase of 50% and 100% in θ_0 results in 4.9% and 1.7% decrease in the sinking velocity, respectively.

Variations in the sinking velocity caused by variations in the initial slab tip length are more significant than the variations in the initial slab dipping angle. A smaller variation in l_0 causes a much higher variation on v_s.

Because two different variations in v_s caused by a change in l_0 for the same θ_0 can be reported, and because the impact of a change in l_0 is not possible to quantify between two experiments with different θ_0, the sinking velocity estimated values are represented on Figure 12 against both the initial slab tip length and angle.

Table 6. Numerical experiments sinking, trench retreat and trailing edge motion velocities. Model and Nature units are summarized. The initial values of l_0 and θ_0 are on Table 2.

	Slab tip			Trench			Trailing edge		
	$\|v_s\|$ [m/s]	$\|v_s\|$ [km/Ma]	r^2	$\|v_t\|$ [m/s]	$\|v_t\|$ [km/Ma]	r^2	$\|v_e\|$ [m/s]	$\|v_e\|$ [km/Ma]	r^2
Num-1	1.82×10^{-4}	25.85	0.9985	2.05×10^{-5}	2.91	0.9530	3.27×10^{-5}	4.65	0.9989
Num-2	1.73×10^{-4}	24.53	0.9984	2.33×10^{-5}	3.31	0.9137	3.94×10^{-5}	5.60	0.9984
Num-3	2.29×10^{-4}	32.48	0.9977	1.68×10^{-5}	2.39	0.9198	2.83×10^{-5}	4.02	0.9929
Num-4	2.25×10^{-4}	31.96	0.9980	2.32×10^{-5}	3.29	0.9601	2.97×10^{-5}	4.21	0.9927
Num-5	2.76×10^{-4}	39.17	0.9955	1.59×10^{-5}	2.26	0.8400	2.73×10^{-5}	3.88	0.9756
Num-6	3.13×10^{-4}	44.41	0.9973	1.70×10^{-5}	2.42	0.8927	3.18×10^{-5}	4.51	0.9899
DM8	3.48×10^{-4}	49.47	0.9807	1.22×10^{-4}	17.38	0.9964	2.00×10^{-4}	28.37	0.9361

Table 7. Linear intervals of the numerical and the DM8 experiments. The time, the slab tip y position and the trench and trailing edge x positions are shown. The subscripts 'i' and 'f' represent the beginning and the end of the interval considered linear, respectively.

	Model units								Nature units							
			Slab tip		Trench		Trailing edge				Slab tip		Trench		Trailing edge	
	t_i [s]	t_f [s]	y_i [m]	y_f [m]	y_i [m]	y_f [m]	x_i [m]	x_f [m]	t_i [Ma]	t_f [Ma]	y_i [km]	y_f [km]	y_i [km]	y_f [km]	x_i [km]	x_f [km]
Num-1	5300	6200	0.176	0.021	0.428	0.447	0.772	0.743	223.9	262.0	1054.6	127.7	2566.6	2682.6	4633.3	4455.6
Num-2	5900	6700	0.168	0.034	0.443	0.462	0.761	0.729	249.3	283.1	1009.1	127.7	2655.3	2771.3	4566.5	4375.4
Num-3	4300	5000	0.174	0.020	0.416	0.429	0.787	0.767	181.7	211.3	1042.0	118.1	2498.3	2573.4	4723.6	4600.7
Num-4	4000	4600	0.167	0.035	0.416	0.430	0.792	0.775	169.0	194.4	1003.5	209.6	2498.3	2580.2	4750.9	4648.4
Num-5	2600	3100	0.174	0.038	0.396	0.405	0.808	0.794	109.8	131.0	1042.3	227.4	2375.4	2430.0	4846.4	4764.5
Num-6	2100	2500	0.157	0.033	0.393	0.400	0.810	0.798	88.7	105.6	939.4	200.8	2356.4	2397.3	4862.6	4787.8
DM8	1500	2280	0.286	0.030	0.391	0.485	0.831	0.676	63.4	96.3	1715.8	178.2	2345.6	2910.0	4985.5	40.53.5

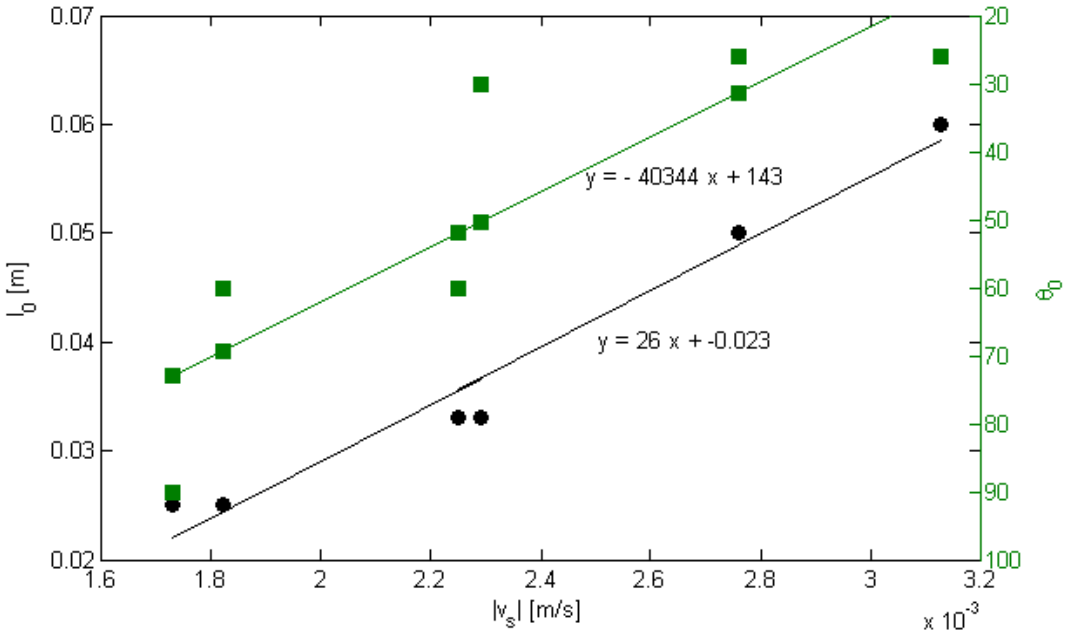

Figure 12. Sinking velocity dependency on initial slab tip length and initial dipping angle comparison. The DM8 experiment is not presented. Linear fitting was performed for both data sets. $r^2 = 0.968$ for l_0 and $r^2 = 0.708$ for θ. Note the the θ axis is reversed.

It is clear that the sinking velocities have almost a linear relation with both variables. Note that the axis on the right is reversed, meaning that the angle has inverse linear relation, as can be proven by the negative slope of the linear regression, also presented on the picture.

4 Discussion

4.1 Slab tip, trench and trailing edge velocity ratios

For all experiments, a theoretical sinking velocity was calculated based on the initial slab tip length and the plate thickness (Table 2), but the estimated sinking velocity values estimated (Tables 3 and 6) are much smaller. The v_s/v_{Stokes}, v_s/v_t, v_s/v_b (only for laboratory experiments) and v_s/v_e (only for numerical experiments) ratios are listed on Table 8.

As already said, the laboratory and numerical results have somewhat different behaviours. For the laboratory experiments the three ratios do not change much, only the v_s/v_{Stokes} ratio seems to depend on initial conditions. Because, in this case the trailing plate is fixed, the v_s/v_t could not be far from one, the plate has to sink and it cannot move horizontally. The v_s/v_t ratio being higher than 1 makes sense because the center, as is was already mentioned, sinks faster since it is less affected by the drag on the mantle. These two ratio do not change much between de laboratory experiments.

For the numerical simulations, the sinking velocity to Stokes velocity ratio varies accordingly with the initial conditions, this ratio gets lower for higher initial length tip and dipping angle. Note

that the DM8 experiment has a ratio closer to the laboratory experiment Lab-1, although the numerical code is set to match this experiment, which is also laboratory, the numerical simulations are not completely in agreement with the laboratory work.

Table 8. Comparisons between Stokes velocity, sinking, trench retreat and trailing edge velocities.

	v_s/v_{Stokes}	v_s/v_t	v_s/v_b[iii]	v_s/v_e[iv]
Lab-1	0.101	0.74	1.13	-
Lab-2	0.125	0.78	1.23	-
Lab-3	0.228	0.79	1.20	-
Num-1	0.071	8.88	-	5.57
Num-2	0.068	7.42	-	4.39
Num-3	0.068	13.63	-	8.09
Num-4	0.067	9.70	-	7.55
Num-5	0.054	17.36	-	10.11
Num-6	0.051	18.41	-	11.02
DM8	0.107	2.85	-	1.74

The v_s/v_t and v_s/v_e ratios show higher values for experiments with higher initial slab tip length, and lower values for experiments with smaller initial slab tip dipping angles. The fact that the trench and trailing edge velocities are so much smaller the sinking velocity of the slab means that the plate is being stretched as the slab is sinking. The higher the ratio the more stretched the plate is at the end. In fact, in figure 7 this effect is visible between experiments Num-1 and Num-6, the two extreme cases.

4.2 Sinking velocity scaling law

The dimensionless velocity dependency on stiffness, initial dipping angle and initial slab tip length proposed by Li & Ribe [2012] (Equation 5) is put to test. They showed that, for values of the stiffness greater than 1, the ratio between the sinking velocity of the center of the slab and the Stokes velocity decreases significantly as S increases. It was also shown that an increase on w/l_0 and H/l_0 ratios increase the dimensionless velocity.

On Table 9 the sinking velocity to Stokes velocity ratio, the stiffness and the ratios w/l_0 and $H/l_0$for each experiment are compared. These dependencies are evaluated separately for the laboratory and the numerical cases because the results have shown very different behaviours between a fixed and a free trailing edge approach.

[iv]Because in the numerical experiments the y position of the slab tip border was not measured, there are only ratios for the laboratory experiments.

[iv]Because in the laboratory experiments the plate was fixed, there are only ratios for the numerical experiments

Table 9. Scaling law for the sinking velocity. Following Li & Ribe [2012], the influence of S, θ_0, w/l_0 and H/l_0 are tested for all experiments.

	v_s/v_{Stokes}	S	θ_0	w/l_0	H/l_0
Lab-1	0.101	4.48	≈ 24	3.83	8.61
Lab-2	0.125	7.90	≈ 20	4.62	10.40
Lab-3	0.228	49.72	≈ 16	8.53	19.20
Num-1	0.071	35.50	60	6.00	15.20
Num-2	0.068	35.50	90	6.00	15.20
Num-3	0.068	15.44	30	4.55	11.52
Num-4	0.067	15.44	60	4.55	11.52
Num-5	0.054	4.44	26	3.00	7.60
Num-6	0.051	2.57	26	2.50	6.33
DM8	0.107	17.12	≈ 30	4.70	11.91

Note that the plate stiffness and the ratios between the plate width and initial slab tip length and between the mantle thickness and the initial slab tip length depend inversely on l_0 (the S definitions is on 6).

The laboratory experiments show that the sinking dimensionless velocity increases as both the initial slab tip length and dipping angle decrease. The maximum increase noted is of 125% between Lab-1 and Lab-3 experiments.

The numerical simulations show a relationship between the dimensionless sinking velocity and initial stiffness but the trend is different from that of Li & Ribe [2012]. Between Num-1 and Num-4 experiments, for a factor of ~ 2.3 increase in S (with the same $\theta_0 = 60°$), there is a increase in the dimensionless sinking velocity by a factor of 1.06 whereas Li & Ribe [2012] has an decrease by a factor 2, for the same variation in S. And between Num-5 and Num-6 experiments (with the same $\theta_0 = 26°$), the differences are similar.

Therefore, the results obtained in this work, using free surface models, show different dependencies from Li & Ribe [2012], which could be explained either by the difference in the geometry: in those calculations the slab was subducting in a half-space or by the lubrication layer used instead of the free surface.

4.3 Comparison with other studies

In three dimensional laboratory experiments with a fixed plate, Funiciello et al. [2003b] observed that the slab starts to subduct freely when it is pushed down between 150 and 200 km, using a analogue model of density contrast of 65 kg/m^3 and viscosity contrast of 1000. But the free subduction they describe was forced, their laboratory experiment utilized a slab geometry that initially had a very long tip. In this work the free subduction happens after the tip has sank around 1000 km below the surface for all laboratory and numerical experiments, see Tables 4 and 7 for the time and depths intervals of the linear fittings.

Schellart [2004] compared fixed and free trailing edge models on the laboratory with a 3-D approach and concluded that slab rollback, slab tip sinking with trench retreat, is enhanced for

a fixed trailing edge condition. It was also observed that the trench migration is significantly suppressed for a free trailing edge plate and the trench and trailing edge displacement curves have similar shapes but the retreat has a higher slope, so trench retreat is faster. Here, the numerical simulations show the opposite, which could be explained by the fact that the comparisons by Schellart [2004] were made on upper mantle models so the system does not evolve enough to reach the steady state analysed here before the slab reaches the bottom.

5 Conclusions

This study has discussed the impact of different initial conditions (l_0 and θ_0) on the slab tip sinking velocity using a set of analogue laboratory experiments, in which the trailing edge of the subducting plate was fixed, and a set of numerical simulations, in which the trailing edge was free to move with the trailing plate. Free and fixed trailing edge models are relevant settings since in Natural systems examples can be found for both cases: a fixed trailing model edge can be compared to scenarios where the trailing plate moves much slower the the retreating trench, for example the Betic-Rif arc [Gutscher et al., 2002], and a free trailing edge model can be compared with systems with a mid-oceanic ridge at one end, e.g., the Nazca plate. Trench and trailing edge displacements and slab geometry time evolution were also discussed and from the obtained results, several conclusions can be drawn.

Dependency of the sinking velocity on the initial conditions is obvious for the free trailing edge case. From the numerical results it is clear that, for a free trailing edge system, the initial slab tip length impacts more the sinking velocity than the initial dipping angle. It was noticed that smaller relative variations on l_0 caused much higher changes in the sinking velocity than the variations on θ_0.

Li & Ribe [2012] have checked the sinking velocity dependency on geometrical parameters using numerical models before, but they used a lubricating layer on top of the plate. Here, dependencies are also verified but with a different trend, and a step further was taken: the numerical simulations presented here were acquired using the free-surface approach, which is more realistic.

The experiments do not take into account an overriding plate, so the estimated velocities are probably overestimated. Duarte et al. [2013] showed that, when a overriding plate is present (more realistic setting), in extreme situations the interplate shear forces could be comparable to the negative buoyancy force that drive the process, which could stall the plate subduction.

Although numerical simulations have been successfully benchmarked with laboratory work using 2-D models before [Schmeling et al., 2008], the 2-D approach is not very realistic, there are effects that are not taken into account like the toroidal mantle flow around the slab lateral border. Here, the numerical results do not quite match the laboratory DM8 experiment, there are possibly effects inherent to laboratory models that are not accounted for on the numerical approach. One possible explanation could be an effect of the surface tension, that maintains the dense plate laid on the surface until the surface tension is locally disrupted when the subduction is initiated by pushing the plate tip down. So, it becomes clear that in three-dimensional models this kind of benchmark is a lot more complex.

An attempt to benchmark laboratory and numerical experiments was made for a free trailing plate. Given the contrast of behaviours of the sinking slab relative to the initial tip conditions for the free trailing plate, the next step is the numerical benchmark of the fixed plate laboratory experiments. This is currently under investigation.

References

Bellahsen, N., Faccenna, C., & Funiciello, F. (2005). Dynamics of subduction and plate motion in laboratory experiments: Insights into the 'plate tectonics" behaviour of the earth. *J. Geophys. Res.*, *110*, B01401. doi: 10.1029/2004JB002999

Conrad, C. P., & Hager, B. H. (1999). Effects of plate bending and fault strengh at subduction zones on plate dynamics. *J. Geophys. Res.*, *104*, 17551-17571.

Duarte, J. C., Schellart, W. P., & Cruden, A. R. (2013). Three-dimensional dynamic laboratory models of subduction with an overrinding plate and variable interplate rheology. *Geophys. J. Int.*. Retrieved from `http://gji.oxfordjournals.org/content/early/2013/07/25/gji.ggt257.abstract` doi: 10.1093/gji/ggt257

Forsyth, D. W., & Uyeda, S. (1975). On the relative importance of the driving forces of plate motion. *Geophys. J. R. Astron. Soc.*, *43*, 163-200.

Funiciello, F., Faccenna, C., Giardini, D., & Regenauer-Lieb, K. (2003b). Dynamics of retreating slabs: 2. Insights from 3-D laboratory experiments. *J. Geophys. Res.*, *108*(B4), 2207. doi: 10.1029/2001JB000896

Funiciello, F., Moroni, M., Piromallo, C., Faccenna, C., Cenedese, A., & Bui, H. A. (2006). Mapping mantle flow during retreating subduction: Laboratory models analyzed by feature tracking. *J. Geophys. Res.*, *111*, B03402. doi: 10.1029/2005JB003792

Funiciello, F., Morra, G., Regenauer-Lieb, K., & Giardini, D. (2003a). Dynamics of retreating slabs: 1. Insights from two-dimensional numeric experiments. *J. Geophys. Res.*, *108*(B4), 2206. doi: 10.1029/2001JB000898

Gutscher, M.-A., Malod, J., Rehault, J.-P., Contrucci, I., Klingelhoefer, F., Mendes-Victor, L., & Spakman, W. (2002). Evidence for active subduction beneath gibraltar. *Geology*, *30*(12), 1071-1074. Retrieved from `http://geology.gsapubs.org/content/30/12/1071.abstract` doi: 10.1130/0091-7613(2002)030<1071:EFASBG>2.0.CO;2

Houseman, G. A., & Gubbins, D. (1997). Deformation of subducted oceanic lithosphere. *Geophysical Journal International*, *131*(3), 535-551. Retrieved from `http://dx.doi.org/10.1111/j.1365-246X.1997.tb06598.x` doi: 10.1111/j.1365-246X.1997.tb06598.x

Jacoby, W. R. (1973). Model experiment of plate movements. *Nature*, *242*, 130-134. doi: 10.1038/physci242130a0

Kaus, B. J. P., Mühlhaus, H., & May, D. A. (2010). A stabilization algorithm for geodynamic numerical simulations with a free surface. *Physics of the Earth and Planetary Interiors*, *181*, 12-20.

Li, Z.-H., & Ribe, N. M. (2012). Dynamics of free subduction from 3-D boundary element modeling. *J. Geophys. Res.*, *117*, B06408. doi: 10.1029/2012JB009165

May, D. A., Brown, J., & Le Pourhiet, L. (2014). *pTatin3D: High-Performance Methods for Long-Term Lithosphere Dynamics, in : Proceedings of ACM/IEEE SC14.*

Ribe, N. M. (2010). Bending mechanics and mode selection in free subduction: a thiin-sheet analysis. *Geophys. J. Int.*, *180*, 559-576.

Schellart, W. P. (2004). Kinematics of subduction and subduction-induced flow in the upper mantle. *J. Geophys. Res.*, *109*(B07401). doi: 10.1029/2004JB002970

Schellart, W. P. (2008). Kinematics and flow patterns in deep mantle and upper mantle subduction models: Influence of the mantle depth and slab to mantle viscosity ratio. *Geochem. Geophys. Geosyst.*, *9*, Q03014. doi: 10.1029/2007GC001656

Schellart, W. P. (2011). Rheology and density of glucose syrupand honey:Determining their suitability for usage in analogue and fluid dynamic models of geological processes. *Journal of Structural Geology*, *33*, 1079-1088.

Schmeling, H., Babeyko, A., Enns, A., Faccenna, C., Funiciello, F., Gerya, T., ... van Hunen, J. (2008). A benchmark comparison of spontaneous subduction models - Towards a free surface. *Physics of the Earth and Planetary Interiors*, *171*, 198-223.

Stegman, D. R., Freeman, J., Schellart, W. P., Moresi, L., & May, D. (2006). Influence of trench width on subduction hinge retreat rates in 3-d models of slab rollback. *Geochem. Geophys. Geosyst.*, *7*, Q03012. doi: 10.1029/2005GC001056

Turcotte, D. L., & Schubert, G. (2002). *Geodynamics* (Second ed.). Cambrigde Universiy Press.

Wilson, J. T. (1965). A new class of faults and their bearing on continental drift. *Nature*, *207*(4995), 343-347. doi: 10.1038/207343a0

Appendix A: Notation used

Table 10. Notation used.

Symbol	Meaning	SI units
a	length scale (sphere)	m
E	energy activation	J·mol^{-1}
F_b	buoyancy force	N
$F_e xt$	external viscous force acting on a bending portion of the plate	N
$F_i nt$	internal viscous force acting on a bending portion of the plate	N
h	thickness of the slab and subducting plate	m
H	mantle thickness	m
H_{box}	box fluid depth	m
g	gravity acceleration	m/s^2
$\mathbf{g}$	gravity vector, $\mathbf{g} = g_x\mathbf{e}_x + g_y\mathbf{e}_y + g_z\mathbf{e}_z$	m/s^2
l	slab tip length	m
l_0	initial slab tip length	m
L	subducting plate length	m
L_{box}	box length	m
P	dynamic pressure	Pa
R	noble gas constant, 8.314472	J·K^{-1}·mol^{-1}
Re	Reynold dimensionless number	
S	stiffness	
T	temperature	$^\circ$ C
t	time	s
t_i	free-subduction initial instant	s
t_f	free-subduction final instant	s
x	position on the xx axis	m
x_i	free-subduction initial x position	m
x_f	free-subduction final x position	m
y	position on the yy axis	m
y_i	free-subduction initial y position	m
y_f	free-subduction final y position	m
y_{min}	minimum depth reached	m
v_e	trailing edge of the plate velocity	m/s
v_b	lateral border slab tip sinking velocity	m/s
v_s	slab tip sinking velocity	m/s
v_t	trench velocity	m/s
v_{Stokes}	Stokes velocity	m/s
V	characteristic velocity	m/s
$\mathbf{v}$	velocity vector, $\mathbf{v} = v_x\mathbf{e}_x + v_y\mathbf{e}_y + v_z\mathbf{e}_z$	m/s
$\mathbf{r}$	position vector, $\mathbf{r} = x\mathbf{e}_x + y\mathbf{e}_y + z\mathbf{e}_z$	m
w	width of the slab and subducting plate	m
W_{box}	box width	m
z	position on the zz axis	m
γ	viscosity ratio, $\gamma = \eta_p/\eta_m$	
η	dynamic viscosity	Pa·s
η_0		Pa·s
η_{ext}	dynamic viscosity of the ambient fluid	Pa·s
η_m	dynamic viscosity of the sub-lithospheric mantle	Pa·s
η_p	dynamic viscosity of the slab and subducting plate	Pa·s

Table 10. Notation used (continuation).

θ	slab dip angle	$^\circ$
θ_0	initial slab dip angle	$^\circ$
ρ	density	kg/m^3
ρ_m	density of the sub-lithospheric mantle	kg/m^3
ρ_p	density of the slab and subducting plate	kg/m^3
$\Delta\rho$	density contrast, $\Delta\rho = \rho_p$ - ρ_m	kg/m^3